ACS APPLIED MATERIALS & INTERFACES

www.acsami.org

Research Article

Promoting Bifunctional Water Splitting by Modification of the Electronic Structure at the Interface of NiFe Layered Double Hydroxide and Ag

Yaming Ma,[#] Dongyu Liu,[#] Hu Wu, Mingtao Li, Shujiang Ding, Anthony Shoji Hall,* and Chunhui Xiao*

Cite This: *ACS Appl. Mater. Interfaces* 2021, 13, 26055−26063

Read Online

ACCESS | Metrics & More | Article Recommendations | Supporting Information

ABSTRACT: Electrochemical water splitting is a promising method for the renewable production of high-purity hydrogen via the hydrogen evolution reaction (HER). Ni−Fe layered double hydroxides (Ni−Fe LDHs) are highly efficient materials for mediating the oxygen evolution reaction (OER), a half-reaction for water splitting at the anode, but LDHs typically display poor HER performance. Here, we report the preparation of self-organized Ag@NiFe layered double hydroxide core-shell electrodes on Ni foam (Ag@NiFe/NF) prepared by galvanic etching for mediating both the HER and OER (bifunctional water-splitting electrocatalysis). This synthetic strategy allowed for the preparation of organized hierarchical architectures which displayed improved the electrochemical performance by tuning the electronic structure of the catalyst and increasing the surface area utilization. X-ray photoelectron spectroscopy (XPS) and theoretical calculations revealed that electron transfer from the Ni−Fe LDH to Ag influenced the adsorption of the reaction intermediates leading to enhanced catalytic activity. The Ag@NiFe/NF electrode displayed overpotentials as low as 180 and 80 mV for oxygen and hydrogen evolution, respectively, at a current density of 10 mA cm^{-2}, and improvements in the specific activity by ∼5× and ∼1.5× for the oxygen and hydrogen evolution reaction, respectively, compared to benchmark NiFe hydroxide materials. Additionally, an integrated water-splitting electrolyzer electrode can be driven by an AA battery.

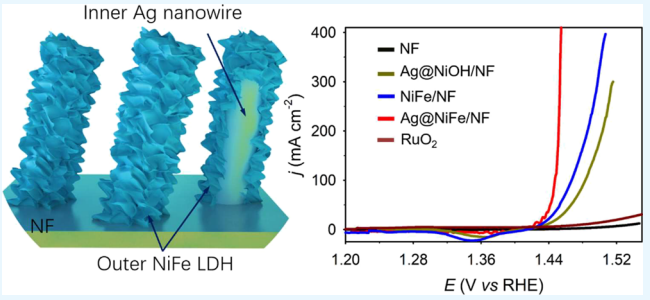

KEYWORDS: *layered double hydroxide, water splitting, electrocatalysis, galvanic exchange, Ag*

INTRODUCTION

Electrochemical water splitting is a promising technology to produce hydrogen, a carbon-neutral fuel, for energy storage and recovery, and a raw material for industrial catalytic applications.[1,2] The water splitting process consists of two primary half-reactions: the anodic oxygen evolution reaction (OER) and cathodic hydrogen evolution reaction (HER). Both reactions need to occur with high efficiency on inexpensive catalysts for water splitting to be a competitive method for the storage of renewable energy in the energy dense bonds of H_2. Currently, state-of-the-art catalysts utilized for both the HER and OER are largely mediated by noble metal-based catalysts, which contain metals such as Pt, Pd, Ru, or Ir; the exorbitant cost and intrinsically poor stability of these materials have hindered the implementation of water electrolysis for energy storage.[3,4] Earth-abundant materials are often found to exhibit a lower activity (on a per site normalized basis) and lower stability than the precious metal catalysts.[5,6] It is paramount to explore inexpensive materials that exhibit catalytic activity comparable[7] or superior to that of conventional noble metal-based materials for overall water splitting while mantaining stability.[8−11]

Recently, 3d transition metal-based compounds, such as metal phosphates and borates, metal phosphides/nitrides/sulfides, layered double hydroxides (LDHs), etc., have demonstrated impressive activity for water splitting.[6,12−16] Among them, Ni-based LDHs have emerged as one of the most interesting materials for water splitting, particularly for the OER, since they are composed of materials that are found naturally on earth, and because they exhibit impressive catalytic activity.[14,17−23] Recent reports have found that doping Ni LDHs with Fe to form NiFe LDHs improved the catalytic activity.[22,24−29] Improved electrical conductivity, more optimal adsorption energy of intermediates, and/or the promotion of

Received: March 19, 2021
Accepted: April 2, 2021
Published: May 26, 2021

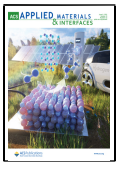

Ni^{3+} oxidation to Ni^{4+} have been suggested to occur when Fe is doped into Ni LDHs.[22,30−32] Alternative strategies to improve activity, such as interfacial engineering, the addition of oxygen vacancies, and/or expanding the basal spacing of the 2D sheets, have also been demonstrated as an effective method to optimize the adsorption energies of active species and improve the mass transport of solution species.[5,33−36] LDH materials are typically insulating in nature; therefore, they require a conductive support to minimize the resistive losses within the material. Several reports have demonstrated that the hybridization of LDH materials with carbon improved the electrical conductivity of the material, affording high catalytic performance. Although LDH materials require supports to exhibit high performance catalysis, utilizing the support material to induce changes in the electronic structure of the LDH by the ligand effect to further improve activity has been largely overlooked. Overall, the aforementioned methods have shown impressive OER performance, but little has been done to allow these materials to serve as bifunctional water splitting catalysts (mediation of both the HER and OER). Furthermore the synthetic strategies used to prepare dispersed LDH materials are slow and costly.

Herein, we systematically investigated NiFe LDHs supported on Ag nanowires (Ag@NiFe LDH) as high performance and stable catalysts for overall water splitting (Scheme 1).

Scheme 1. Schematic Illustrating the Fabrication Route of the 3D Ag@NiFe/NF Electrode

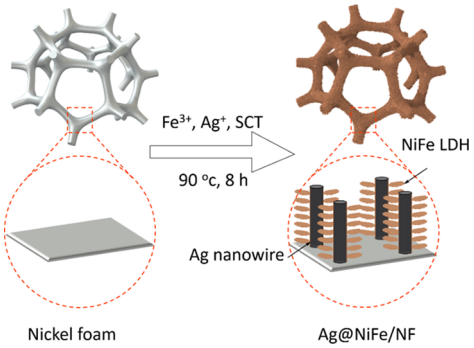

The growth of NiFe LDHs onto Ag nanowires modulated the electronic properties of the LDHs via catalyst−support interactions, improving the catalytic activity of this material for both the HER and OER. The preparation of the Ag @NiFe LDH occurred in a single step by galvanic etching of Ni foam (NF) with Ag^+ and Fe^{2+}, enabling the rapid formation of a self-organized nanostructure. Overall, this method provides several advantages over conventional methods, which are slow and require several synthetic steps. In this method, the potential difference between the metal current collector and ions allowed for material fabrication without the need for expensive reagents (e.g., binder) or harsh reaction conditions (high temperature/pressure or electric field).[37,38] The hierarchical morphology produced by galvanic etching allowed the Ag@NiFe LDH to exhibit several advantages relative to the 2D NiFe LDH: (1) The high surface area improved material utilization and increased the density of catalytic activity sites. Meanwhile, the superhydrophilic nanosheets and open pores improved the mass transport of reactant species and facilitated the exchange of products with fresh reactants; (2) the Ag nanowire-based core in the NiFe LDH shell provided a fast electron transport pathway, dramatically enhancing the conductivity and reducing the charge transfer resistance of the NiFe LDH; (3) interfacial electron redistribution of the Ag@NiFe LDH occurred on the interface, which influenced the adsorption of the active species (OH*; H*) and improved the catalytic activity. This resulting Ag@NiFe/NF electrode exhibited excellent activity for both OER and HER, requiring overpotentials as low as 180 and 78 mV to reach 10 mA cm^{-2}, respectively, while maintaning excellent durability.

The materials prepared by galvanic etching of nickel foam (NF) with aqueous solution containing Fe^{3+} and Ag^+ were characterized by scanning electron microscopy (SEM) and transmission electron microscopy (TEM). The NF displayed a brown color after being etched in a Ag^+- and Fe^{3+}-containing solution, while the NF appeared brownish-red when etched in an Fe^{3+}-containing solution (Figure S1). Porous rodlike structures were observed to be grown throughout the NF surface with abundant, open pores among the nanorods. The diameter and length of nanorods were found to be 60 and 900 nm, respectively (Figure 1a−c). A low-magnification TEM image revealed hierarchical structural organization; we observed sheetlike structures, which decorated a dense nanowire core (Figure 1d). The thin sheetlike structures were transparent to the electrons, indicating that the materials consisted of thin lamellae. The high-resolution TEM (HRTEM) image revealed that the atomic spacing of atoms within the core was 0.236 nm, which can be indexed to the (111) facet of Ag, and the corresponding fast Fourier transformation pattern of the exposed core revealed the existence of the (111) planes (Figure 1e,f). Furthermore, a distance of 0.24 nm was measured from the high-angle annular dark-field imaging image, which also confirmed the existence of the (111) facet of Ag (Figure S2a). These results were supported by X-ray diffraction (XRD), which displayed diffraction peaks that corresponded to the crystalline structure of metallic silver, noting that the peaks from Ni are from the NF substrate (Figure 1g). HRTEM showed that the thin shell was composed of an amorphous material, which covered the metallic Ag nanowire; this was further confirmed by the lack of significant XRD peaks from other materials apart from Ni and Ag. Scanning transmission electron microscopy and elemental mapping of the composite structure indicated that the amorphous material consists of Ni, Fe, and O, which were homogeneously distributed over Ag (Figure 1h). The Fe/Ni atomic ratio was 1.04:1 as determined by energy-dispersive X-ray spectroscopy (Figure S2), which was similar to that reported for the NiFe LDH.[5,39] Taken together, we concluded that the materials consisted of a Ag nanowire core covered by an amorphous or poorly crystalline phase of the NiFe LDH.

X-ray photoelectron spectroscopy (XPS) was performed to measure the surface composition and the electronic interaction between the core and shell of Ag@NiFe/NF. The peak positions were calibrated by the C 1 s peak at 284.6 eV.[40] XPS survey scans for Ag@NiFe/NF showed that elemental Ag was present when Ag^+ was added to the etching solution (Figure 2a). The Ni 2P spectrum from Ag@NiFe/NF showed two characteristic peaks at 855.2 and 872.7 eV for the $2p_{3/2}/2p_{2/1}$ doublet of Ni^{2+} and corresponding shakeup satellites peaks (denoted as Sat.).[21,41] The Fe 2p spectral features of Ag@NiFe/NF displayed two prominent peaks at 712.6 and 722.4 eV, which can been attributed to $2p_{3/2}$ and $2p_{1/2}$ spin orbits of Fe^{3+} (Figure 2c).[20,42−44] Ni^0 was not observed since XPS is a surface-sensitive technique; the elemental Ni from the NF was

https://doi.org/10.1021/acsami.1c05123
ACS Appl. Mater. Interfaces 2021, 13, 26055−26063

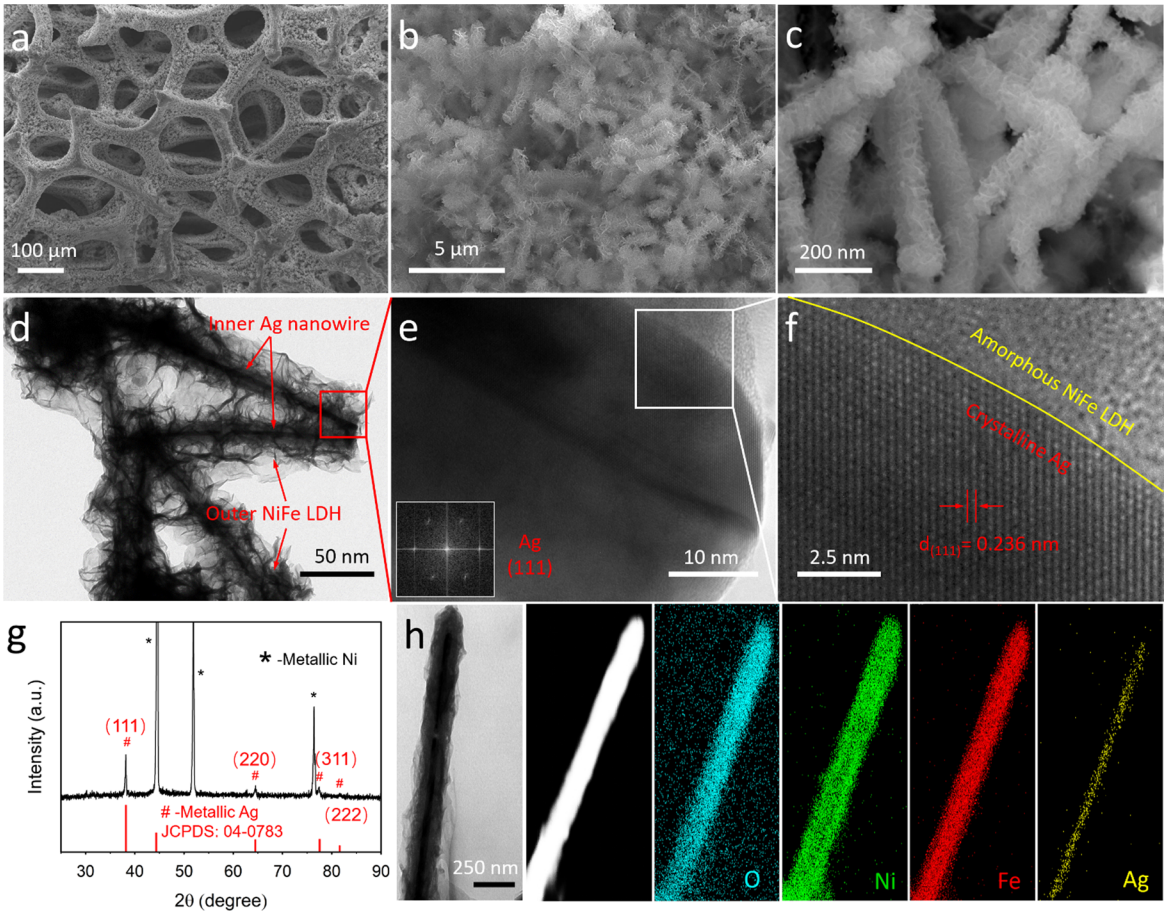

Figure 1. Structural characterization of Ag@NiFe/NF. (a, b, and c) SEM, (d, e, and f) TEM, (g) XRD, and (h) HAADF image with elemental mapping. gg and HAADF STEM image of a single nanowire.

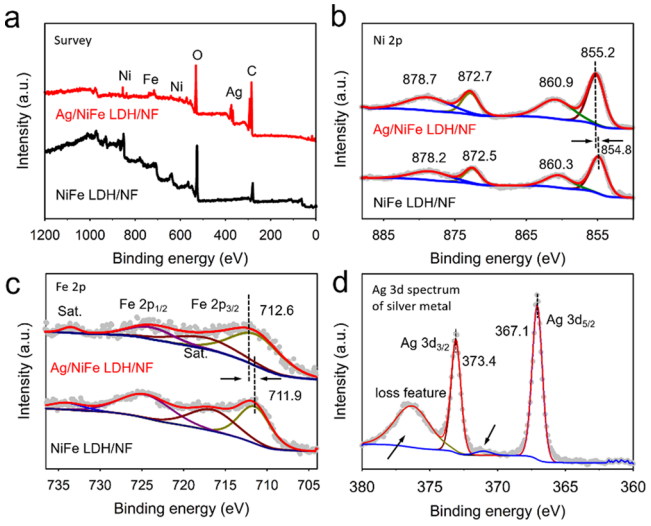

Figure 2. XPS (a) survey scan, and high resolution spectra of (b) Ni 2p, (c) Fe 2p, and (d) Ag 3d region of Ag@NiFe/NF.

buried under Ag and the LDH. As revealed in Figure 2d, the Ag 3d spectrum displayed two characteristic peaks at 367.1 and 373.4 eV which can be assigned to silver metal; however, these values are shifted negatively by ∼1 eV, indicating increased electron density.[33,45] Compared to pristine NiFe/NF, the fundamental Ni 2p and Fe 2p peaks of Ag@NiFe/NF were shifted positively by ∼0.4−0.7 eV when metallic Ag was present, suggesting a reduction of electron density on the Ni and Fe sites. The transfer of electrons from the NiFe LDH to Ag metal occurred because of differences in the Fermi levels between these materials. The hole accumulation on the NiFe LDH and electron accumulation on the Ag metal should be beneficial for enhancing the OER or HER, respectively.

To uncover the growth mechanism of Ag@NiFe/NF, the Nernst equation was used to analyze the redox potential of the ions used in galvanic etching:

$$Ag^{+} + e = Ag(s)\ E^{o} = 0.799\ V$$

$$Fe^{3+} + e = Fe^{2+}\ E^{o} = 0.771\ V$$

$$Ni^{2+} + 2e = Ni(s)\ E^{o} = 0.257\ V$$

$$O_2 + 2H_2O + 4e = 4OH^{-}\ E^{o} = 1.230\ V$$

According to the Nernst equation a larger potential difference between ions will increase the driving force for galvanic exchange.[46,47] The following equations were used, under nonstandard thermodynamic conditions, to calculate the driving force for galvanic exchange: $\Delta_r G_m = -nFE$ and $E = E^{o} - 0.0592\lg(a_{Red}/a_{Ox})$. The $\Delta_r G_m$ for the exchange of Ag^{+} and Fe^{3+} with Ni was −60.94 and −62.98 kJmol^{-1}, respectively, which indicated that the reaction between the ions with the NF was spontaneous at room temperature. The synthetic process was divided into two steps; first, the surface of the Ni NF skeleton was oxidized and subsequently etched by the Ag^{+} and Fe^{3+} ions, leading to the deposition of metallic Ag and the

https://doi.org/10.1021/acsami.1c05123
ACS Appl. Mater. Interfaces 2021, 13, 26055−26063

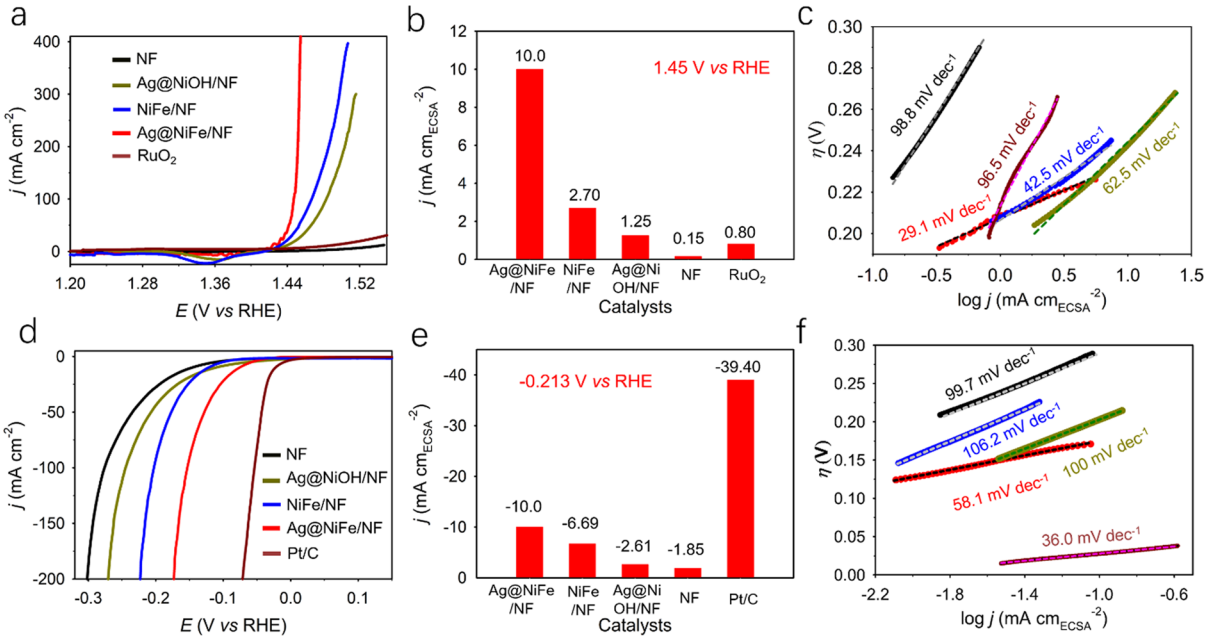

Figure 3. (a) Liner sweep voltammograms (LSVs) of NF, Ag@NiOH/NF, Ag@NiFe/NF, NiFe/NF, and RuO_2 electrodes displaying the OER performance, (b) specific activity at 1.45 V vs RHE, and (c) Tafel slopes. (d) LSVs of the electrodes displaying the HER performance, (e) specific activity at −0.213 V vs RHE, and (f) Tafel slopes. All measurements were performed in 1 M KOH and LSVs were collected at a scan rate of 5 mV/s.

formation of Fe^{2+} and Ni^{2+}. This initial reaction occurred because the reduction potential of Ni to Ni^{2+}, $E^{o}_{Ni/Ni2+}$ (0.257), is more negative than the reduction potentials of Fe^{3+} to Fe^{2+}, $E^{o}_{Fe3+/Fe2+}$ (0.771 V), and Ag^{+} to Ag, $E^{o}_{Ag+/Ag}$ (0.799 V). The Fe^{2+} that was formed in the prior step can reduce oxygen with water serving as a proton source, forming OH^{-} and Fe^{3+}. The OH^{-} built up at the interface will react with interfacial Fe^{3+} and Ni^{2+}, leading to the precipitation of the NiFe LDH over the NF and Ag. The Ni^{2+} and Fe^{3+} ions deposit as NiFe LDHs at the on the surface of the NF skeleton since mass transport away from the NF is slow under quiescent conditions. A temperature of 90 °C was selected to accelerate the reaction rate.

$$Ag^{+} + Ni(s) \rightarrow Ag(s) + Ni^{2+} \quad (1)$$

$$2Fe^{3+} + Ni(s) \rightarrow 2Fe^{2+} + Ni^{2+} \quad (2)$$

$$4Fe^{2+} + O_2 + 2H_2O \rightarrow 4Fe^{3+} + 4OH^{-} \quad (3)$$

$$Ni^{2+} + Fe^{3+} + xOH^{-} \rightarrow NiFe(OH)_x \quad (4)$$

The electrocatalytic performance for the OER and HER was performed in a typical three-electrode configuration in 1 M KOH electrolyte. The voltage was scanned cathodically from high potentials to low potentials at a 5 mV s^{-1} scan rate to avoid an overlap between Ni^{2+}/Ni^{3+} oxidation with OER current and provide reliable electrochemical data (Figure 3). The onset potential for the OER was 1.39 V for Ag@NiFe/NF, which was significantly more negative than NiFe/NF (1.41 V), Ag@NiOH/NF (1.43 V), and the bare NF (1.45 V). The OER performance was evaluated by measuring the overpotential required to reach 10 and 100 mA cm^{-2} as these current densities are relevant to solar fuel synthesis (Figure 3 and Figure S3b).[6] The voltage required to reach 10 and 100 mA cm^{-2} on Ag@NiFe/NF electrodes was 1.42 and 1.44 V, respectively, were significantly lower than NiFe/NF (1.43 V @ 10 mA cm^{-2}; 1.46 V @ 100 mA cm^{-2}), Ag@NiOH/NF (1.45 V @ 10 mA cm^{-2}; 1.50 V @ 100 mA cm^{-2}), and bare NF (1.53 V @ 10 mA cm^{-2}; 1.70 V @ 100 mA cm^{-2}). Moreover, the Ag@NiFe/NF exhibited high stability under galvanostatic conditions over the course of 12 h (Figure S4). The low onset potentials and low overpotentials needed to reach 10 and 100 mA cm^{-2} revealed that Ag@NiFe/NF is a potential catalyst for the OER.

To directly compare the intrinsic performance of all the catalysts, the specific activity was measured by normalizing the current by the electrochemistry active surface area (ECSA), which was estimated from the double-layer capacitance (Figure 3b and Figure S4a). The specific activity at 1.45 V was 10 mA cm^{-2}_{ECSA} for Ag@NiFe/NF, which was significantly higher than Ag@NiOH/NF (2.64 mA cm^{-2}_{ECSA}), NiOH/NF (1.18 mA cm^{-2}_{ECSA}), and bare NF (0.134 mA cm^{-2}_{ECSA}). The ∼5 to 10-fold enhancement of the specific activity for the OER on Ag@NiFe/NF relative to the other catalysts indicated that the Ag supports improved the activity of NiFe/NF.

To provide insights on to the high catalytic performance of Ag@NiFe/NF, we calculated the Tafel slopes ($b = \frac{dE}{d\log(j)}$), which were measured by quasi-steady state LSVs (Figure 3). The aggregate rate constant of an electrochemical reaction is dependent on both the exchange current density, i_o, and the transfer coefficient, $\alpha = \frac{2.303RT}{F}\left(\frac{dE}{d\log(j)}\right)^{-1}$, as shown in eq 1, where R is the universal gas constant, F is Faraday's constant, T is the temperature (in 298 K), and η is the overpotential:

$$i = i_o e^{\alpha\eta F/RT}$$

Both the α and i_o values can be derived from the inverse of b and the extrapolation of b to 0 overpotential, respectively. The i_0 provides information regarding the intrinsic rate of electron transfer at equilibrium (η = 0), while α provides information about the number of electrons transferred between the resting

https://doi.org/10.1021/acsami.1c05123
ACS Appl. Mater. Interfaces 2021, 13, 26055−26063

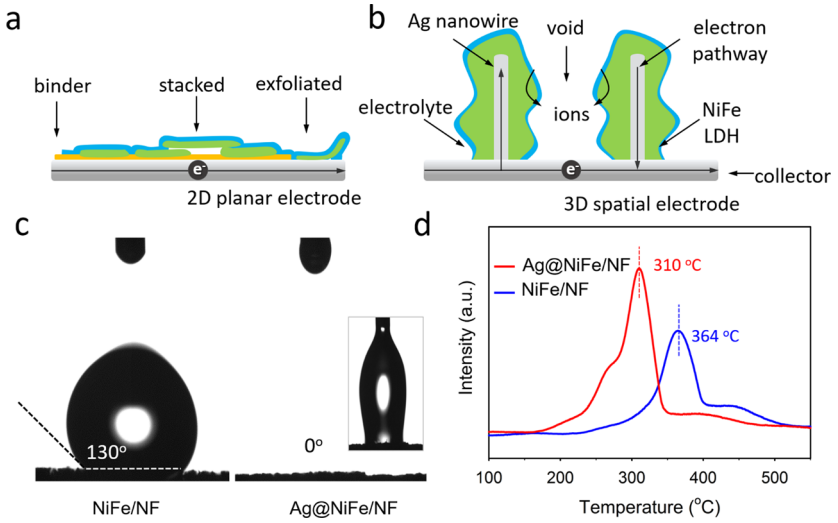

Figure 4. Schematic of (a) 2D planar electrode and (b) 3D architected electrode. (c) Contact angle measurements and (d) O_2-TPD spectra of NiFe/NF and Ag@NiFe/NF electrodes.

state and the rate-limiting step of the catalytic cycle and the fraction of the interfacial potential that lowers the free energy barrier of the reaction. Therefore, a larger α value is desirable from a kinetic perspective as a smaller change in the applied voltage will cause a larger increase in the reaction rate. Ag@NiFe/NF displayed a b value of ∼27 mV dec^{-1}, which was lower than the other catalysts, which displayed b varying from ∼40 to 100 mV dec^{-1}; corresponding to a α value of ∼3 for Ag@NiFe/NF and ∼ 0.6 to 1.5 for the other catalysts (Figure 3C). The i_0 value of Ag@NiFe/NF was 9.2 × 10^{-4}, which was higher than the i_0 value of Ag@NiOH/NF (1.1 × 10^{-4}), NiFe/NF (7.4 × 10^{-4}), and NF (1.1× 10^{-5}).

The charge transfer resistance

$$R_{ct} = \frac{b}{j}$$

where j is the measured current at a constant voltage, and b is the Tafel slope. The R_{ct} was evaluated by electrochemical impedance spectroscopy (EIS) at a constant voltage under catalytic conditions and fitted to an equivalent circuit model (Figure S3c). An R_{ct} of 0.64 Ω was measured at 1.55 V for Ag@NiFe/NF, which was lower than NiFe/NF (1.88 Ω), Ag@NiOH/NF (0.99 Ω), and NF (5.24 Ω). The values of the R_{ct} are proportional to b, therefore it is inversely proportional to α, indicating an agreement between the R_{ct} and α measured by EIS and the Butler−Volmer equation at high overpotential. The low R_{ct}, large α and i_0 suggested that the improved electrical conductivity and electron redistribution via metal−support interactions improved the reaction kinetics of the Ag@NiFe/NF relative to other catalysts.

We assessed the HER performance in 1 M KOH with LSVs collected at 5 mV s^{-1} to demonstrate that our materials can be utilized as an efficient catalyst for overall water splitting. The HER onset potential for Ag@NiFe/NF was −0.026 V, which was significantly more positive than NiFe/NF (−0.032 V), Ag@NiOH/NF (−0.035 V), and bare NF (−0.068 V). (Figure 3d). The overpotentials required to reach −10 and −100 mA cm^{-2} on Ag@NiFe/NF electrodes were −0.078 and −0.153 V, which was significantly lower than NiFe/NF (−0.125 V @ −10 mA cm^{-2}; −0.203 V @ −100 mA cm^{-2}), Ag@NiOH/NF (−0.117 V @ −10 mA cm^{-2}; −0.244 V @ −100 mA cm^{-2}), and the bare NF (−0.130 V @ −10 mA cm^{-2}; −0.248 V @ −100 mA cm^{-2}), respectively. Moreover, the Ag@NiFe/NF exhibited high stability under galvanostatic conditions, as indicated by long-term chronoamperometry over the course of 12 h (Figure S4). Kinetic measurements revealed that Ag@NiFe/NF displayed a b value of ∼60 mV dec^{-1}, which was lower than the other catalysts which displayed b values of ∼100 mV dec^{-1}, corresponding to α values of ∼1 and ∼0.6, respectively (Figure 3f). The i_0 value of Ag@NiFe/NF was 7.3 × 10^{-4}, which was higher than the i_0 of Ag@NiOH/NF (1.2 × 10^{-4}), NiFe/NF (3.4 × 10^{-4}), and NF (2.4 × 10^{-5}). The R_{ct} value for Ag@NiFe/NF was 1.15 Ω, which was smaller than NiFe/NF (1.28 Ω), Ag@NiOH/NF (1.4 Ω), and NF (2.14 Ω) (Figure S3f). Taken together, we can establish that the kinetics for the HER were significantly improved on Ag@NiFe/NF by metal−support interactions and improved electrical conductivity, allowing it to possess superior specific activity relative to the benchmark LDH catalysts.

To gain insight into the enhanced kinetics for the catalytic performance of the Ag@NiFe/NF electrodes grown by galvanic etching, we evaluated the morphology of our material vs conventional electrodes fabricated by solution casting (Figure 4). The electrodes prepared by conventional methods suffered from restacking of the 2D materials; which decreased the accessible surface area, and reduced electrical conductivity from insulating binders, resulting in poor electrocatalytic activity. The 3D structure of Ag@NiFe/LDH increased the space utilization; which improved electrolyte accessibility and increased the ECSA. Contact angle measurements (Figure 4c and Video S1 and Vedio S2) showed a contact angle of 0° on 3D Ag@NiFe/NF; indicating that the nanostructured morphology improved the solvent wettability, resulting in a super hydrophilic surface. The superhydrophilicity of the Ag@NiFe/NF electrode substantially improved the HER and OER kinetics by increasing the contact area of the catalyst with H_2O, which is a reactant for both reactions. In addition to the superhydrophilicity, the Ag nanowire provided a low resistance electron pathway and modified the electron density on the catalyst surface, leading to reduced charge transfer resistance. We evaluated the chemisorption O_2 on the 2D NiFe/NF electrode and 3D Ag@NiFe/NF electrode by the temperature-programmed-desorption method (Figure 4d). The temper-

https://doi.org/10.1021/acsami.1c05123
ACS Appl. Mater. Interfaces 2021, 13, 26055−26063

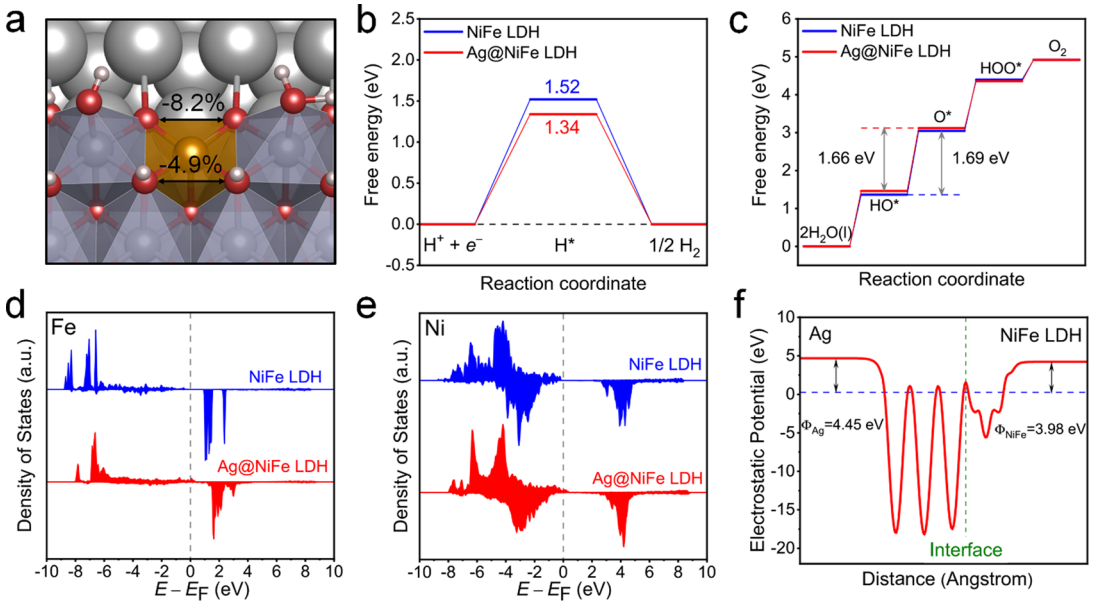

Figure 5. DFT calculations. (a) Top view of the Ag@NiFe surface model, and the lattice distortion was compared with the pristine NiFe LDH. Color scheme for chemical representation: yellow for Fe, purple for Ni, gray for Ag, red for O, and white for H. Energy diagrams for (b) HER and (c) OER on NiFe and Ag@NiFe. (d, e) Element-projected density of states for Fe and Ni in NiFe, and Ag@NiFe surface models. (f) Electrostatic potential along the z axis of the Ag@NiFe complex.

ature of the O_2 desorption peak increased from 310 °C for the 3D Ag@NiFe/NF electrode to 364 °C for the 2D NiFe/NF electrode; the decreased temperature for O_2 desorption on Ag@NiFe/NF indicated a weaker adsorption energy of O_2 relative to 2D NiFe/NF. This result is significant for two reasons: (1) lower O_2 adsorption energy on the NiFe LDH, should improve the catalytic activity since prior reports show that the O_2 adsorption is too strong on these materials,[48] and (2) decreased O_2 adsorption will improve the removal of O_2 bubbles from the electrode surface at OER high current densities. Furthermore, the construction of abundant open voids among nanorods can decrease the chemisorption abilities by enlarging the bubble contact angle resulting in reduced adhesion force and improved bubble release.[49,50] In brief, the 3D spatial electrode allowed for improved electronic properties from metal−support interactions, and enhanced electrolyte infiltration and quick release of gas from the 3D morphology.

Theoretical calculations based on density functional theory (DFT) were performed to determine the impact of the Ag core on the electrocatalytic performance. Figure 5a displays the top view of the NiFe LDH edge site on the Ag (111) surface. Due to the lattice constant mismatch (2.88 Å for Ag and 3.14 Å for the NiFe LDH), the Fe−O polyhedral (yellow region) would be slightly depressed and the local environment of active site Fe would be modified. To evaluate the impact on catalysis performance, the ΔG ($|\Delta G_{H^*}| = 0$) values for HER and OER were calculated (Figure 5b,c). It was found that the free energy change of the limiting steps were reduced for both reactions, which indicated higher catalytic activity. The HER performance improvement was greater than for the OER; this result was consistent with the experimental catalytic performance (Figure 3c and Figure 5g). In addition, we noticed that the H* adsorption was enhanced, while the HO* and O* adsorption weakened, and the HOO* adsorption strength almost maintained. To clarify the differences between the activity enhancement for both half reactions, the element-projected densities of states (DOS) of Fe and Ni atoms were calculated (Figure 5d,e). For Fe, some partly occupied states appeared around the Fermi level after coming into contact with Ag. The states above the Fermi level could act as a shallow electron acceptor to facilitate the charge transfer from adsorbates to the electrode, enhancing the H* adsorption, while the extra states below the Fermi level would reduce the energy and weaken the Fe−O interaction. Meanwhile, the DOS showed that the Fermi level would cross the valance band for both Fe and Ni, suggesting an electronic conductivity improvement for the NiFe LDH. Moreover, the electrostatic potential plotted in Figure 5f showed that the NiFe LDH possessed a smaller work function than Ag, which would cause electrons to be transferred from the NiFe LDH to Ag, which was consistent with the binding energy shifts measured by XPS (Figure 2). Taken together, these results indicated the importance of the interfacial electron redistribution between the NiFe LDH and the support on tuning the adsorption energy of key intermediates for the HER and OER.

The practical application of the 3D Ag@NiFe/NF for full water splitting electrolysis device was evaluated by utilizing 3D Ag@NiFe/NF serving as both the cathode and anode in a two-electrode electrolysis cell (Figure 6). LSVs revealed that the electrolysis device exhibited high performance, reaching 10 mA cm^{-2} at a cell potential of 1.56 V. The long-term stability of the

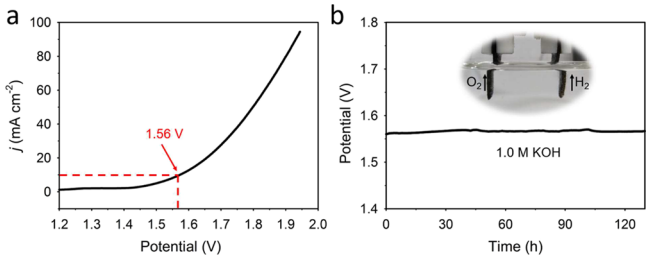

Figure 6. (a) LSV and (b) long-term stability at 10 mA cm^{-2} of the Ag@NiFe/NF electrode in a two-electrode cell.

https://doi.org/10.1021/acsami.1c05123
ACS Appl. Mater. Interfaces 2021, 13, 26055−26063

device was assessed by galvanostatic measurements at 10 mA cm^{-2}. The 3D Ag@NiFe/NF electrolyzer showed excellent activity and stability, delivering a current density of 10 mA cm^{-2} while maintaining a cell voltage of ~1.56 V for more than 130 h (Figure 3l). Our catalyst exhibited among the highest performance compared to bifunctional water-splitting electrocatalysts reported in other literature studies (Table S1). Because of the impressively low onset potential for the electrolyzer, even below 1.37 V, the water electrolysis could be driven by a single-cell AA battery with a nominal voltage of ~1.5 V. Large quantities of H_2 and O_2 bubbles can be observed on the surfaces of the electrodes (Figure S6). These results unambiguously demonstrated the excellent catalytic activity of the 3D Ag@NiFe/NF and its great potential as an efficient bifunctional water-splitting electrocatalyst.

CONCLUSIONS

In summary, a hierarchical 3D Ag/NiFe hydroxide core-shell electrode fabricated by galvanic etching exhibited excellent activity for bifunctional water water splitting in alkaline electrolytes. The electron redistribution in Ag@NiFe on the interface was verified by the XPS, O_2 TPD, and DFT calculations. The improved adsorption energies of the active species (OH*; H*) enhanced the HER and OER performance. The open porosity and binder-free architecture of our system provided abundant catalytic sites, efficient electron/mass transfer, and efficient gas release. The as-prepared Ag@NiFe/NF electrode exhibited overpotentials as low as 180 and 80 mV to deliver 10 mA cm^{-2} for the OER and HER. An electrolyzer using Ag@NiFe/NF as both the cathode and anode required a low voltage of 1.52 V to obtain 10 $mAcm^{-2}$ and can be powered by an AA battery with an output voltage of 1.5 V. We demonstrated that galvanic etching is a facile strategy to create unique interfacial architectures for high performance electrotalysis.

ASSOCIATED CONTENT

Supporting Information

The Supporting Information is available free of charge at https://pubs.acs.org/doi/10.1021/acsami.1c05123.

Digital image of samples; characterization of Ag@NiFe/NF; polarization curves; durability of the as-obtained Ag@NiFe/NF; C_{dl} measurement; digital image of the water-splitting device; experimental and calculation methods; and comparisons of electrocatalytic activity (PDF)

Contact angle measurement of Ag @ NiFe LDH (MP4)

Contact angle measurement of NiFe LDH (MP4)

AUTHOR INFORMATION

Corresponding Authors

Anthony Shoji Hall − *Department of Materials Science and Engineering, Johns Hopkins University, Baltimore, Maryland 21218, United States*; Email: shoji@jhu.edu

Chunhui Xiao − *Xi'an Key Laboratory of Sustainable Energy Materials Chemistry, Department of Applied Chemistry, School of Chemistry, Xi'an Jiaotong University, Xi'an 710049, China; Shaanxi Quantong Joint Research Institute of New Energy Vehicles Power, Xi'an Jiaotong University, Xi'an 710049, China;* orcid.org/0000-0001-7451-5099; Email: chunhuixiao@xjtu.edu.cn

Authors

Yaming Ma − *Xi'an Key Laboratory of Sustainable Energy Materials Chemistry, Department of Applied Chemistry, School of Chemistry, Xi'an Jiaotong University, Xi'an 710049, China; Department of Materials Science and Engineering, Johns Hopkins University, Baltimore, Maryland 21218, United States*

Dongyu Liu − *International Research Center for Renewable Energy, State Key Laboratory of Multiphase Flow in Power Engineering, Xi'an Jiaotong University, Xi'an 710049, China*

Hu Wu − *Xi'an Key Laboratory of Sustainable Energy Materials Chemistry, Department of Applied Chemistry, School of Chemistry, Xi'an Jiaotong University, Xi'an 710049, China*

Mingtao Li − *International Research Center for Renewable Energy, State Key Laboratory of Multiphase Flow in Power Engineering, Xi'an Jiaotong University, Xi'an 710049, China*

Shujiang Ding − *Xi'an Key Laboratory of Sustainable Energy Materials Chemistry, Department of Applied Chemistry, School of Chemistry, Xi'an Jiaotong University, Xi'an 710049, China; Shaanxi Quantong Joint Research Institute of New Energy Vehicles Power, Xi'an Jiaotong University, Xi'an 710049, China;* orcid.org/0000-0002-5683-0973

Complete contact information is available at: https://pubs.acs.org/10.1021/acsami.1c05123

Author Contributions

#Denotes co-first authors.

Notes

The authors declare no competing financial interest.

ACKNOWLEDGMENTS

We greatly appreciate the financial support from the Key Laboratory Construction Program of Xi'an Municipal Bureau of Science and Technology (201805056ZD7CG40), the National Natural Science Foundation of China (21405119), and the Natural Science Basic Research Plan in Shaanxi Province of China (2015JQ2046). China Postdoctoral Science Foundation (2014 M562392) and Fundamental Research Funds for the Central Universities (08143099) are gratefully acknowledged. We thank Mr. Ren (Instrument Analysis Centre of Xi'an Jiao Tong University) for the valuable help with the test. A.S.H. acknowledges financial support from the National Science Foundation under award NO. CHE-1764310 and the Sloan Foundation.

REFERENCES

(1) Hwang, J.; Rao, R. R.; Giordano, L.; Katayama, Y.; Yu, Y.; Shao-Horn, Y. Perovskites in Catalysis and Electrocatalysis. *Science* **2017**, *358*, 751−756.

(2) Blöchl, P. E. Projector Augmented-Wave Method. *Phys. Rev. B* **1994**, *50*, 17953.

(3) Su, J.; Ge, R.; Jiang, K.; Dong, Y.; Hao, F.; Tian, Z.; Chen, G.; Chen, L. Assembling Ultrasmall Copper-Doped Ruthenium Oxide Nanocrystals into Hollow Porous Polyhedra: Highly Robust Electrocatalysts for Oxygen Evolution in Acidic Media. *Adv. Mater.* **2018**, *30*, No. 1801351.

(4) Wang, H.; Lee, H.-W.; Deng, Y.; Lu, Z.; Hsu, P.-C.; Liu, Y.; Lin, D.; Cui, Y. Bifunctional Non-noble Metal Oxide nanoparticle Electrocatalysts through Lithium-induced Conversion for overall water splitting. *Nat. Commun.* **2015**, *6*, 7261.

(5) Liu, Y.; Liang, X.; Gu, L.; Zhang, Y.; Li, G.-D.; Zou, X.; Chen, J.-S. Corrosion Engineering towards Efficient Oxygen Evolution

Electrodes with Stable Catalytic Activity for over 6000 hours. *Nat. Commun.* **2018**, *9*, 2609.
(6) Luo, J.; Im, J.-H.; Mayer, M. T.; Schreier, M.; Nazeeruddin, M. K.; Park, N.-G.; Tilley, S. D.; Fan, H. J.; Grätzel, M. Water Photolysis at 12.3% Efficiency via Perovskite Photovoltaics and Earth-Abundant Catalysts. *Science* **2014**, *345*, 1593−1596.
(7) Kanan, M. W.; Surendranath, Y.; Nocera, D. G. Cobalt-Phosphate Oxygen-Evolving Compound. *Chem. Soc. Rev.* **2009**, *38*, 109−114.
(8) Bo, Z.; De Luna, L. Y.; Janmohamed, P.; Xin, A.; Yang, H. L.; Vojvodic, H.; Sargent, A.; Edward, H. Homogeneously dispersed multimetal oxygen-evolving catalysts. *Science* **2016**, *352*, 333−337.
(9) Hu, B.-C.; Wu, Z.-Y.; Chu, S.-Q.; Zhu, H.-W.; Liang, H.-W.; Zhang, J.; Yu, S.-H. SiO_2-protected Shell Mediated Templating Synthesis of Fe−N-doped Carbon Nanofibers and Their Enhanced Oxygen Reduction Reaction Performance. *Energy Environ. Sci.* **2018**, *11*, 2208−2215.
(10) Zhang, W.; Peng, Q.; Shi, L.; Yao, Q.; Wang, X.; Yu, A.; Chen, Z.; Fu, Y. Merging Single-Atom-Dispersed Iron and Graphitic Carbon Nitride to a Joint Electronic System for High-Efficiency Photocatalytic Hydrogen Evolution. *Small* **2019**, *15*, No. 1905166.
(11) Baricuatro, J. H.; Saadi, F. H.; Carim, A. I.; Velazquez, J. M.; Kim, Y.-G.; Soriaga, M. P. Influence of Redox-Inactive Cations on the Structure and Electrochemical Reactivity of Synthetic Birnessite, a Heterogeneous Analog for the Oxygen-Evolving Complex. *J. Phys. Chem. C* **2016**, *120*, 15618−15631.
(12) Jin, S. Are Metal Chalcogenides, Nitrides, and Phosphides Oxygen Evolution Catalysts or Bifunctional Catalysts? *ACS Energy Lett.* **2017**, *2*, 1937−1938.
(13) Li, W.; Xiong, D.; Gao, X.; Liu, L. The Oxygen Evolution Reaction Enabled by Transition Metal Phosphide and Chalcogenide Pre-catalysts with Dynamic Changes. *Chem. Commun.* **2019**, *55*, 8744−8763.
(14) Gong, M.; Li, Y.; Wang, H.; Liang, Y.; Wu, J. Z.; Zhou, J.; Wang, J.; Regier, T.; Wei, F.; Dai, H. An Advanced Ni−Fe Layered Double Hydroxide Electrocatalyst for Water Oxidation. *J. Am. Chem. Soc.* **2013**, *135*, 8452−8455.
(15) Dresp, S.; Dionigi, F.; Klingenhof, M.; Strasser, P. Direct Electrolytic Splitting of Seawater: Opportunities and Challenges. *ACS Energy Lett.* **2019**, *4*, 933−942.
(16) Weiß, S.; Ertl, M.; Varhade, S. D.; Radha, A. V.; Schuhmann, W.; Breu, J.; Andronescu, C. Trivalent Iron Rich CoFe Layered Oxyhydroxides for Electrochemical Water Oxidation. *Electrochim. Acta* **2020**, No. 136256.
(17) Zhao, B.; Zhang, L.; Zhen, D.; Yoo, S.; Ding, Y.; Chen, D.; Chen, Y.; Zhang, Q.; Doyle, B.; Xiong, X.; Liu, M. A Tailored Double Perovskite Nanofiber Catalyst Enables Ultrafast Oxygen Evolution. *Nat. Commun.* **2017**, *8*, No. 14586.
(18) Xiao, H.; Shin, H.; Goddard, W. A., III Synergy Between Fe and Ni in the Optimal Performance of (Ni,Fe)OOH Catalysts for the Oxygen Evolution Reaction. *PNAS* **2018**, *115*, 5872−5877.
(19) Niu, S.; Jiang, W.-J.; Wei, Z.; Tang, T.; Ma, J.; Hu, J.-S.; Wan, L.-J. Se-Doping Activates FeOOH for Cost-Effective and Efficient Electrochemical Water Oxidation. *J. Am. Chem. Soc.* **2019**, *141*, 7005−7013.
(20) Yu, L.; Yang, J. F.; Guan, B. Y.; Lu, Y.; Lou, X. W. D. Hierarchical Hollow Nanoprisms Based on Ultrathin Ni-Fe Layered Double Hydroxide Nanosheets with Enhanced Electrocatalytic Activity towards Oxygen Evolution. *Angew. Chem., Int. Ed.* **2018**, *57*, 172−176.
(21) Wang, Y.; Xie, C.; Zhang, Z.; Liu, D.; Chen, R.; Wang, S. In Situ Exfoliated, N-Doped, and Edge-Rich Ultrathin Layered Double Hydroxides Nanosheets for Oxygen Evolution Reaction. *Adv. Funct. Mater.* **2018**, *28*, No. 1703363.
(22) Yang, Y.; Dang, L.; Shearer, M. J.; Sheng, H.; Li, W.; Chen, J.; Xiao, P.; Zhang, Y.; Hamers, R. J.; Jin, S. Highly Active Trimetallic NiFeCr Layered Double Hydroxide Electrocatalysts for Oxygen Evolution Reaction. *Adv. Energy Mater.* **2018**, *8*, No. 1703189.
(23) Liu, J.; Wang, J.; Zhang, B.; Ruan, Y.; Lv, L.; Ji, X.; Xu, K.; Miao, L.; Jiang, J. Hierarchical $NiCo_2S_4$@NiFe LDH Heterostructures Supported on Nickel Foam for Enhanced Overall-Water-Splitting Activity. *ACS Appl. Mater. Interfaces* **2017**, *9*, 15364−15372.
(24) Feng, J. X.; Xu, H.; Dong, Y. T.; Lu, X. F.; Tong, Y. X.; Li, G. R. Efficient Hydrogen Evolution Electrocatalysis Using Cobalt Nanotubes Decorated with Titanium Dioxide Nanodots. *Angew. Chem., Int. Ed.* **2017**, *56*, 2960−2964.
(25) Yu, M.; Wang, Z.; Liu, J.; Sun, F.; Yang, P.; Qiu, J. A Hierarchically Porous and Hydrophilic 3D Nickel-iron/MXene electrode for Accelerating Oxygen and Hydrogen Evolution at High Current Densities. *Nano Energy* **2019**, *63*, No. 103880.
(26) Zhou, J.; Yu, L.; Zhu, Q.; Huang, C.; Yu, Y. Defective and Ultrathin NiFe LDH Nanosheets Decorated on V-doped Ni_3S_2 Nanorod Arrays: a 3D Core-shell Electrocatalyst for Efficient Water Oxidation. *J. Mater. Chem. A* **2019**, *7*, 18118−18125.
(27) Zhang, A.; He, R.; Li, H.; Chen, Y.; Kong, T.; Li, K.; Ju, H.; Zhu, J.; Zhu, W.; Zeng, J. Nickel Doping in Atomically Thin Tin Disulfide Nanosheets Enables Highly Efficient CO_2 Reduction. *Angew. Chem., Int. Ed.* **2018**, *57*, 10954−10958.
(28) Fan, K.; Chen, H.; Ji, Y.; Huang, H.; Claesson, P. M.; Daniel, Q.; Philippe, B.; Rensmo, H.; Li, F.; Luo, Y.; Sun, L. Nickel−vanadium monolayer double hydroxide for efficient electrochemical water oxidation. *Nat. Commun.* **2016**, *7*, No. 11981.
(29) Bu, Y.; Nam, G.; Kim, S.; Choi, K.; Zhong, Q.; Lee, J.; Qin, Y.; Cho, J.; Kim, G. A Tailored Bifunctional Electrocatalyst: Boosting Oxygen Reduction/Evolution Catalysis via Electron Transfer Between N-Doped Graphene and Perovskite Oxides. *Small* **2018**, *14*, No. 1802767.
(30) Lin, J.; Wang, P.; Wang, H.; Li, C.; Si, X.; Qi, J.; Cao, J.; Zhong, Z.; Fei, W.; Feng, J. Defect-Rich Heterogeneous MoS_2/NiS_2 Nanosheets Electrocatalysts for Efficient Overall Water Splitting. *Adv. Sci.* **2019**, *6*, No. 1900246.
(31) Feng, J. X.; Ye, S. H.; Xu, H.; Tong, Y. X.; Li, G. R. Design and Synthesis of FeOOH/CeO_2 Heterolayered Nanotube Electrocatalysts for the Oxygen Evolution Reaction. *Adv. Mater.* **2016**, *28*, 4698−4703.
(32) Zhang, X.; Zhao, Y.; Zhao, Y.; Shi, R.; Waterhouse, G. I. N.; Zhang, T. A Simple Synthetic Strategy toward Defect-Rich Porous Monolayer NiFe-Layered Double Hydroxide Nanosheets for Efficient Electrocatalytic Water Oxidation. *Adv. Energy Mater.* **2019**, *9*, No. 1900881.
(33) Song, C.; Zhao, Z.; Sun, X.; Zhou, Y.; Wang, Y.; Wang, D. In Situ Growth of Ag Nanodots Decorated Cu_2O Porous Nanobelts Networks on Copper Foam for Efficient HER Electrocatalysis. *Small* **2019**, *15*, No. 1804268.
(34) Zhua, W.; Zhang, T.; Zhanga, Y.; Yuea, Z.; Lia, Y.; Wanga, R.; Jia, Y.; Sunb, X.; Wanga, J. A Practical-oriented NiFe-based Water-oxidation Catalyst Enabled by Ambient Redox and Hydrolysis co-Precipitation strategy. *Appl. Catal. B: Environ.* **2018**, *244*, 844−852.
(35) Yu, L.; Zhou, H.; Sun, J.; Qin, F.; Yu, F.; Bao, J.; Yu, Y.; Chen, S.; Ren, Z. Cu Nanowires Shelled with NiFe Layered Double Hydroxide Nanosheets as Bifunctional Electrocatalysts for Overall Water Splitting. *Energy Environ. Sci.* **2017**, *10*, 1820−1827.
(36) Yu, L.; Zhou, H.; Sun, J.; Mishra, I. K.; Luo, D.; Yu, F.; Yu, Y.; Chen, S.; Ren, Z. Amorphous NiFe Layered Double Hydroxide Nanosheets Decorated on 3D Nickel Phosphide Nanoarrays: a Hierarchical Core-shell Electrocatalyst for Efficient Oxygen Evolution. *J. Mater. Chem. A* **2018**, *6*, 13619−13623.
(37) Ya, M.; Zhi, W.; Zhang, B.; Yang, Z.; Shu, D.; Chun, X. Galvanic-replacement Mediated Synthesis of Copper−Nickel Nitrides as Electrocatalyst for Hydrogen Evolution Reaction. *J. Mater. Chem. A* **2017**, *5*, 24850−24858.
(38) Li, M.; Zhao, Z.; Cheng, T.; Fortunelli, A.; Chen, C.-Y.; Yu, R.; Zhang, Q.; Gu, L.; Merinov, B. V.; Lin, Z.; Zhu, E.; Yu, T.; Jia, Q.; Guo, J.; Zhang, L.; Goddard, W. A.; Huang, Y.; Duan, X. Ultrafine Jagged Platinum Nanowires Enable Ultrahigh Mass Activity for the Oxygen Reduction Reaction. *Science* **2016**, *354*, 1414−1419.

https://doi.org/10.1021/acsami.1c05123
ACS Appl. Mater. Interfaces 2021, 13, 26055−26063

(39) Wu, Z.; Wang, Z.; Geng, F. Radially Aligned Hierarchical Nickel/nickel-Iron (Oxy)hydroxide Nanotubes for Efficient Electrocatalytic Water Splitting. *ACS Appl. Mater. Interfaces* **2018**, *10*, 8585−8593.
(40) Han, L.; Dong, S.; Wang, E. Transition-Metal (Co, Ni, and Fe)-Based Electrocatalysts for the Water Oxidation Reaction. *Adv. Mater.* **2016**, *28*, 9266−9291.
(41) Liu, J.; Zhu, D.; Ling, T.; Vasileff, A.; Qiao, S.-Z. S-$NiFe_2O_4$ ultra-small nanoparticle built nanosheets for efficient water splitting in alkaline and neutral pH. *Nano Energy* **2017**, *40*, 264−273.
(42) Zhou, Y.; Zeng, H. C. 3D Networks of CoFePi with Hierarchical Porosity for Effective OER Electrocatalysis. *Small* **2018**, *14*, No. 1704403.
(43) Zou, S.; Burke, M. S.; Kast, M. G.; Fan, J.; Danilovic, N.; Boettcher, S. W. Fe (Oxy)hydroxide Oxygen Evolution Reaction Electrocatalysis: Intrinsic Activity and the Roles of Electrical Conductivity, Substrate, and Dissolution. *Chem. Mater.* **2015**, *27*, 8011−8020.
(44) Yeo, B. S.; Bell, A. T. Enhanced Activity of Gold-Supported Cobalt Oxide for the Electrochemical Evolution of Oxygen. *J. Am. Chem. Soc.* **2011**, *133*, 5587−5593.
(45) Cai, Z.; Zhou, D.; Wang, M.; Bak, S. M.; Wu, Y.; Wu, Z.; Tian, Y.; Xiong, X.; Li, Y.; Liu, W.; Siahrostami, S.; Kuang, Y.; Yang, X. Q.; Duan, H.; Feng, Z.; Wang, H.; Sun, X. Introducing Fe(2+) into Nickel-Iron Layered Double Hydroxide: Local Structure Modulated Water Oxidation Activity. *Angew. Chem., Int. Ed.* **2018**, *57*, 9392−9396.
(46) Walczak, M. M.; Dryer, D. A.; Jacobson, D. D.; Foss, M. G.; Flynn, N. T. pH-Dependent Redox Couple: Illustrating the Nernst Equation Using Cyclic Voltammetry. *J. Chem. Educ.* **1997**, *74*, No. 1195.
(47) Sheng, P.; Sakuraba, Y.; Lau, Y.-C.; Takahashi, S.; Mitani, S.; Hayashi, M. The spin Nernst effect in tungsten. *Sci. Adv.* **2017**, *3*, No. 1701503.
(48) Jin, H.; Mao, S.; Zhan, G.; Xu, F.; Bao, X.; Wang, Y. Fe incorporated α-$Co(OH)_2$ nanosheets with remarkably improved activity towards the oxygen evolution reaction. *J. Mater. Chem. A* **2017**, *5*, 1078−1084.
(49) Xu, W.; Lu, Z.; Sun, X.; Jiang, L.; Duan, X. Superwetting Electrodes for Gas-Involving Electrocatalysis. *Acc. Chem. Res.* **2018**, *51*, 1590−1598.
(50) Li, Y.; Zhang, H.; Xu, T.; Lu, Z.; Wu, X.; Wan, P.; Sun, X.; Jiang, L. Under-Water Superaerophobic Pine-Shaped Pt Nanoarray Electrode for Ultrahigh-Performance Hydrogen Evolution. *Adv. Funct. Mater.* **2015**, *25*, 1737−1744.

https://doi.org/10.1021/acsami.1c05123
ACS Appl. Mater. Interfaces 2021, 13, 26055−26063